

Molecular modeling of freezing of simple fluids confined within carbon nanotubes

Francisco R. Hung,^{a)} Benoit Coasne,^{b)} Erik E. Santiso, and Keith E. Gubbins

*Department of Chemical and Biomolecular Engineering,
North Carolina State University, Raleigh, North Carolina 27695-7905*

Flor R. Siperstein

*Departament d'Enginyeria Quimica, Universitat Rovira i Virgili, Campus Sescelades, Avenida dels Països
Catalans 26, 43007, Tarragona, Spain*

Malgorzata Sliwinska-Bartkowiak

Institute of Physics, Adam Mickiewicz University, Umultowska 85, 61-614 Poznan, Poland

(Received 27 December 2004; accepted 2 February 2005; published online 13 April 2005)

We report Monte Carlo simulation results for freezing of Lennard-Jones carbon tetrachloride confined within model multiwalled carbon nanotubes of different diameters. The structure and thermodynamic stability of the confined phases, as well as the transition temperatures, were determined from parallel tempering grand canonical Monte Carlo simulations and free-energy calculations. The simulations show that the adsorbate forms concentric molecular layers that solidify into defective quasi-two-dimensional hexagonal crystals. Freezing in such concentric layers occurs via intermediate phases that show remnants of hexatic behavior, similar to the freezing mechanism observed for slit pores in previous works. The adsorbate molecules in the inner regions of the pore also exhibit changes in their properties upon reduction of temperature. The structural changes in the different regions of adsorbate occur at temperatures above or below the bulk freezing point, depending on pore diameter and distance of the adsorbate molecules from the pore wall. The simulations show evidence of a rich phase behavior in confinement; a number of phases, some of them inhomogeneous, were observed for the pore sizes considered. The multiple transition temperatures obtained from the simulations were found to be in good agreement with recent dielectric relaxation spectroscopy experiments for CCl_4 confined within multiwalled carbon nanotubes. © 2005 American Institute of Physics. [DOI: 10.1063/1.1881072]

I. INTRODUCTION

Confinement within a porous material is known to lead to a number of novel phenomena involving solid-fluid phase behavior.¹⁻³ Such phenomena can have practical applications in adhesion, lubrication, frost heaving, nanofabrication, and characterization of porous materials. From a fundamental viewpoint, studies of freezing and melting of confined systems can provide important insights on the effect of confinement, surface forces, and reduced dimensionality on phase transitions. Most of the experimental studies of freezing in confinement have been carried out for a wide variety of adsorbates in silica materials (mainly MCM-41, SBA-15, and Vycor glass) with different pore sizes.¹⁻³ The freezing temperature inside the pore was found to be lower than that for the bulk, with the depression becoming larger as the pore size decreased, in agreement with the Gibbs–Thomson equation. Nevertheless, this macroscopic equation was found to break down for systems confined in pores of small sizes, below a few adsorbate molecular diameters.¹⁻³ Significant

hysteresis effects were observed, as well as evidence of different freezing behaviors for the adsorbate in the central regions of the pore and the contact layer (the adsorbed molecules adjacent to the pore wall), suggesting the presence of inhomogeneous confined phases. In most cases, the structure of the confined solid was found to deviate from the bulk crystal phase: below certain pore sizes the adsorbate crystallized only partially, and for smaller pores an amorphous solid phase was always observed.

This large amount of experimental evidence clearly indicates that the phase diagram of a substance can be significantly altered when confined within a porous material. These results also suggest that the freezing temperature inside the pore is lower than that for the bulk. Nevertheless, simulation and experimental studies have shown that an elevation in the freezing point is observed for systems where the adsorbate-wall interactions are strong compared to the adsorbate-adsorbate interactions, and there is matching between the morphologies of the porous media and the confined solid phase. For instance, Klein and Kumacheva⁴ studied cyclohexane and octamethylcyclotetrasiloxane (OMCTS) confined between parallel mica plates in a surface force apparatus (SFA). Upon reduction of the separation between the surfaces, it was observed that the confined films could sustain a finite shear stress for macroscopic times, and the film rigidity

^{a)} Author to whom correspondence should be addressed; electronic mail: frhung@unity.ncsu.edu

^{b)} Present address: Laboratoire de Physicochimie de la Matière Condensée (UMR CNRS 5617), Université de Montpellier II, Place Eugène Bataillon, 34095 Montpellier, Cedex 5, France.

(quantified by an “effective viscosity”) increased. This was interpreted as a liquid to solid phase transition occurring at temperatures well above the bulk freezing point. In addition, a number of experiments using activated carbon fibers (ACFs) have reported that the freezing temperature in confinement may be lower (water,^{5–7} octanol,⁸ and undecanol⁸) or higher (methanol,⁷ carbon tetrachloride,⁹ benzene,¹⁰ aniline,¹¹ OMCTS,¹² and cyclohexane¹²) than the bulk value; in some cases (nitrobenzene¹³), no appreciable change in the freezing temperature was observed.

Miyahara and Gubbins¹⁴ performed systematic grand canonical Monte Carlo (GCMC) simulations of freezing and melting of Lennard-Jones (LJ) methane confined within slit pores. When the adsorbate-wall interactions were weaker compared to the adsorbate-adsorbate interactions, the freezing temperature in confinement was significantly lower than in the bulk, as reported in most of the experiments for silica pores. In contrast, a large increase in the freezing temperature was found for strongly attractive materials, such as porous carbons. No appreciable change in the freezing temperature was observed when the adsorbate-wall and adsorbate-adsorbate interactions were similar. Moreover, the contact layers were found to freeze at temperatures higher or lower than the rest of the adsorbed fluid for the cases of strongly or weakly attractive walls, respectively. Those findings were further confirmed in simulation studies where the free energy of the confined phases was calculated, using a thermodynamic integration method¹⁵ and a Landau–Ginzburg approach.^{16,17} By combining the latter approach with corresponding states theory, Radhakrishnan *et al.*^{13,17} obtained phase diagrams for a wide range of adsorbates and slit pore walls, in terms of the pore width H and a parameter α measuring the ratio of the adsorbate-wall to adsorbate-adsorbate attractive interaction. Recent simulations^{17,18} and experiments¹⁸ for CCl_4 within ACFs have suggested the existence of hexatic phases in temperature ranges between those for the hexagonal crystal and liquid phases. Such hexatic phases are quasi-two-dimensional (2D) systems with quasilong-range sixfold bond orientational order and positional disorder. The liquid-hexatic and hexatic-crystal transitions for the molecular layers of adsorbate were found¹⁸ to be consistent with the Kosterlitz–Thouless–Halperin–Nelson–Young (KTHNY) theory for 2D melting.^{19–21}

For pores of cylindrical geometries, Maddox and Gubbins²² investigated freezing of confined LJ methane using a combined GCMC and molecular dynamics (MD) simulation approach, obtaining similar conclusions as in the study by Miyahara and Gubbins.¹⁴ The freezing temperatures in cylindrical pores were found to be lower than those obtained within slit pores of similar characteristics, due to the additional degree of confinement. Kanda *et al.*²³ also studied freezing of LJ methane within model carbon cylindrical pores by means of GCMC simulations, finding a nonmonotonic dependence of freezing point against pore diameter. This was interpreted as a result of the competition between geometric constraints and fluid-wall interaction effects. Sliwinska-Bartkowiak *et al.*²⁴ reported both experimental and simulation results for freezing of nitrobenzene and CCl_4 in porous glasses and MCM-41. It was found that the con-

finer fluid is able to crystallize when the average pore diameter D is greater than $20\sigma_{ff}$, where σ_{ff} is the size parameter of the adsorbate. For smaller pore diameters, the confined fluid solidifies forming either frustrated crystals or amorphous solids. Hoffmann and Nielaba²⁵ performed classical and path-integral Monte Carlo simulations in the canonical (NVT) ensemble to study the freezing of argon and neon within cylindrical pores. For strongly attractive pores, the adsorbate was found to freeze in concentric layers, with the contact layer freezing at temperatures higher than the rest of the system. Structures with local fcc or hcp order were observed for pores with weak fluid-wall interactions. Hung *et al.*²⁶ and Sliwinska-Bartkowiak *et al.*²⁷ presented results from parallel tempering grand canonical Monte Carlo simulations and dielectric relaxation spectroscopy experiments, for nitrobenzene and carbon tetrachloride confined within multiwalled carbon nanotubes with an internal diameter of 5 nm. The results suggested the presence of inhomogeneous phases, composed of combinations of crystalline and liquid regions within the pore over extended temperature ranges. Good agreement was found between the simulation results and the experimental measurements of transition temperatures.

In this work, we aim at obtaining a rigorous picture of the solid-fluid phase behavior of LJ carbon tetrachloride (CCl_4) confined within structureless multiwalled carbon nanotubes (MWCNTs) of $D \leq 5$ nm. The freezing behavior of the adsorbate is investigated by means of parallel tempering grand canonical Monte Carlo (PT-GCMC) simulations. For the largest MWCNT considered ($D=5$ nm), we also performed free-energy calculations²⁸ in order to rigorously determine the range of thermodynamic stability of each phase and establish the values of the thermodynamic transition temperatures. The Landau and grand free energies are determined by using a spatially inhomogeneous order parameter,^{13,17} composed of a group of several variables quantifying crystallinity in different regions of the pore. Finally, we also present results from grand canonical parallel tempering simulations for the same adsorbate within two smaller MWCNTs, $D=3.9$ nm and $D=2.8$ nm.

II. SIMULATION DETAILS

A. Models

Carbon tetrachloride was modeled using the LJ (12, 6) potential, with parameters fitted¹⁷ to reproduce the bulk freezing point and liquid density at bulk coexistence: $\sigma_{ff} = 0.514$ nm, $\epsilon_{ff}/k_B = 366.1$ K. The LJ potential was cut and shifted at a distance of $5\sigma_{ff}$. The multiwalled carbon nanotube was modeled as a structureless, cylindrical pore of density ρ_w , using the potential of Peterson *et al.*,²⁹ so that CCl_4 could only be adsorbed inside the nanotube. The potential parameters for the carbon nanotube were chosen to be equal to those of graphite:^{30,31} $\rho_w = 114$ nm⁻³, $\sigma_{ww} = 0.340$ nm, and $\epsilon_{ww}/k_B = 28.0$ K. The Lorentz–Berthelot mixing rules were used to calculate the cross parameters σ_{fw} and ϵ_{fw} . Modeling the carbon nanotube walls as a structureless solid is expected to be a good approximation, since the size parameter of LJ CCl_4 (0.514 nm) is much larger than the C–C bond length in

the carbon nanotubes (0.14 nm), and therefore the effect of surface corrugation is expected to be small. A previous simulation work¹⁴ on freezing/melting of LJ methane ($\sigma_{ff} = 0.381$ nm) confined within graphitic slit pores showed quantitatively similar results for both smooth and structured walls.

A cylindrical simulation box with reduced pore diameter $D^* = D/\sigma_{ff}$ was considered, and periodic boundary conditions were used at both ends. Three different diameters were studied: $D^* = 9.7, 7.5,$ and 5.5 (corresponding to $D = 5.0, 3.9,$ and 2.8 nm, respectively). The reduced cylindrical pore length $L^* = L/\sigma_{ff}$ was fixed at $L^* = 60$, since previous simulations^{17,18} of freezing of LJ CCl₄ within slit pores have shown that fluctuations do not destroy the ordered phases for system sizes with $L^* \geq 60$.

B. Methods

In our simulation runs we followed previous works^{14,16,26,27} in choosing sets of temperature and chemical potential (T, μ) such that $\mu(T)$ corresponds to the liquid/vapor or solid/vapor coexistence pressure $P(T)$. Such a path implies that the confined phase is always in equilibrium with a saturated vapor in the bulk. The properties of the LJ fluid at coexistence were obtained elsewhere.³²

We have used the parallel tempering scheme in the grand canonical ensemble, as proposed by Yan and de Pablo,³³ to determine the equilibrium properties of the adsorbate within the three pore sizes considered. In this method, a GCMC simulation is performed simultaneously in n noninteracting replicas with volume V , each one at a different set of values of (T, μ) . Standard GCMC trial moves are attempted at random with equal probability in each one of the replicas. In addition, configuration swaps are randomly attempted between pairs of replicas, subject to specific acceptance criteria.³³ These swap moves provide an effective way to deal with metastability problems and improve phase space sampling. Cell lists³⁴ were used to speed up the simulation runs, and typical systems had 2800–3800 particles for $D^* = 9.7$, 1700–2200 molecules for $D^* = 7.5$, and 900–1100 particles for $D^* = 5.5$. Thermodynamic properties were averaged over a minimum of 400 million MC steps; however, much longer runs were used for most of the sets of (T, μ) studied, especially near the transition points for the larger pore diameters.

In our PT-GCMC simulations, we started from well-equilibrated liquidlike and solidlike configurations obtained from previous GCMC runs at different temperatures. Then, we assigned these configurations randomly to each set of (T, μ) , letting the systems equilibrate. For consistency, we repeated the simulations for $D^* = 9.7$ using a different set of initial configurations, obtaining similar results. In order to cover all the phase space of interest and guarantee frequent swaps between replicas, the number of replicas used in a single run was 50 for $D^* = 9.7$, 28 for $D^* = 7.5$, and 32 for $D^* = 5.5$, corresponding to $\Delta T = 2, 4,$ and 5 K, respectively, between adjacent replicas. The evolution of the PT-GCMC simulation as a function of the number of Monte Carlo steps was monitored and, after equilibration, it was verified that

each configuration visited many sets of (T, μ) along a single simulation run. The acceptance ratio for exchanging configurations was not completely uniform between all the replicas, meaning that the selected conditions of (T, μ) were not optimal and could be further refined. It has been reported³⁵ that the acceptance probability for swapping moves in a parallel tempering algorithm can be made uniform between all the replicas, by selecting temperature intervals such that all adjacent temperatures are in a fixed ratio. We have not attempted to do that in our simulations. Nevertheless, the ratio T_{i+1}/T_i and μ_{i+1}/μ_i in our simulations had small variations (between 1.01 and 1.03 for T and 1.005 and 1.006 for μ); in addition, the fraction of accepted swap moves was over 30% for all the replicas, which is considered satisfactory for a parallel tempering simulation.^{33,36,37}

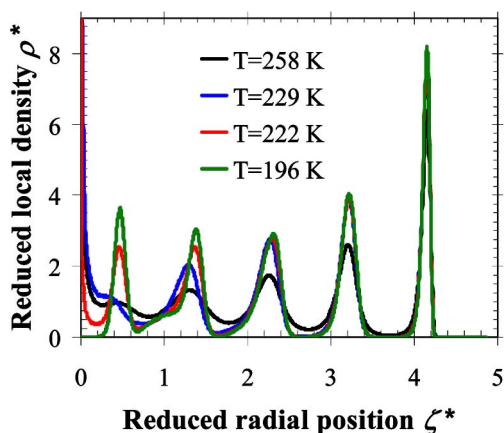
C. Structure analysis

In our previous works,^{26,27} it was found that LJ CCl₄ confined within a MWCNT of $D^* = 9.7$ did not solidify into three-dimensional (3D) crystalline structures commonly observed in bulk phases, in agreement with previous studies.^{22–25} We can expect the same behavior for smaller pore diameters since the geometrical constraints will be more important. Significant ordering into distinct concentric molecular layers was found for the three pore diameters considered. This is concluded from the analysis of molecular configuration snapshots and the local-density profile in the radial direction,²³

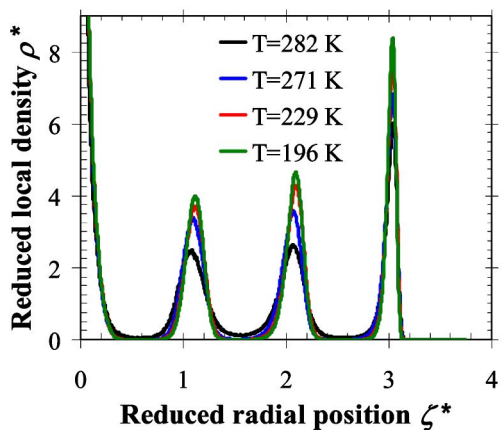
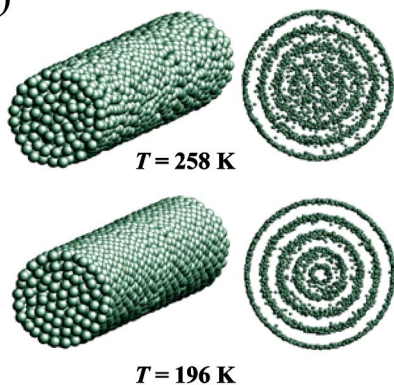
$$\rho^*(\zeta) = \frac{\langle N(\zeta) \rangle}{L\pi[(\zeta + \Delta\zeta/2)^2 - (\zeta - \Delta\zeta/2)^2]}, \quad (1)$$

where $N(\zeta)$ is the number of particles with radial coordinate ζ between $(\zeta - \Delta\zeta/2)$ and $(\zeta + \Delta\zeta/2)$. The local-density profile of the adsorbed phase along the radial direction is shown in Fig. 1 at several temperatures, for $D^* = 9.7$ and 7.5 . The maxima in each peak increase and the interpeak minima decrease as the temperature is reduced, indicating a well-defined layer separation. For $D^* = 9.7$, the density profile at temperatures higher than 229 K exhibits four concentric layers (annuli) of adsorbate and a highly localized quasirow of particles at the center of the pore; however, five annuli of adsorbate molecules are observed in the density profile at lower temperatures. In contrast, for $D^* = 7.5$ there are three annuli of particles and a quasirow of molecules at the center of the pore, for the whole range of temperatures studied. These observations are corroborated by the snapshots presented in Fig. 1. The density profile for $D^* = 5.5$ (not shown) exhibits two concentric layers and a center quasirow of molecules for all the temperatures studied, a similar behavior to that observed for $D^* = 7.5$.

A representative quasi-2D configuration of the molecules within a layer j can be obtained by cutting the layer along the axial direction z and unrolling it flat. To study the freezing behavior of each layer, we have followed the methodology of previous works^{16,38} in measuring bond order parameters that were sensitive to the degree of crystallinity in the system. First, we identified the nearest neighbors of a given particle i as those molecules k that were in the same layer, and within



(a)



(b)

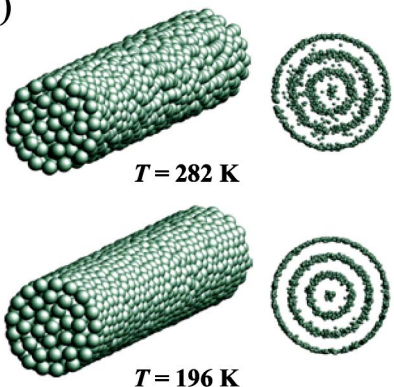


FIG. 1. Density profile along the radial direction, and snapshots of typical configurations of LJ CCl_4 confined within structureless MWCNT, at different temperatures and different diameters: (a) $D^* = 9.7$; (b) $D^* = 7.5$. The carbon walls are not shown in the snapshots for clarity. Front views of the same snapshots depicting the adsorbed molecules with a reduced diameter are also provided to help visualize the formation of concentric layers as the temperature decreases.

a distance $r_b = 1.3\sigma_{ff}$ from particle i .¹⁶ This distance corresponds to the first minimum of the radial distribution function in a fcc crystal at bulk coexistence. The vectors \mathbf{r}_{ik} joining the neighbors are called “bonds.” The orientation of such bonds with respect to an arbitrary axis is given by the angle θ_k . Then, the average 2D bond orientational order parameter $\Phi_{6,j}$ of layer j can be determined as,^{17,20}

$$\Phi_{6,j} = \langle |\Psi_{6,j}(\mathbf{r})| \rangle, \quad (2)$$

$$\Psi_{6,j}(\mathbf{r}) = \frac{1}{N_b} \sum_{k=1}^{N_b} \exp(i6\theta_k), \quad (3)$$

where N_b is the number of nearest-neighbor bonds. The local bond order parameter $\Psi_{6,j}(\mathbf{r})$ measures the hexagonal crystalline bond order of a given molecule at a position \mathbf{r} within layer j . We expect $\Phi_{6,j} = 1$ when the layer has the structure of a perfect, 2D hexagonal crystal and $\Phi_{6,j} = 0$ when the layer has a 2D liquidlike structure (in the thermodynamic limit).

We also monitored the two-dimensional, in-plane positional, and orientational pair-correlation functions within each layer j . The positional pair-correlation function $g_j(r)$ is given by the common radial distribution function measured within the 2D plane formed by each unwrapped layer j , r being the in-layer distance. The orientational pair-correlation function $G_{6,j}(r)$ measures correlations between the local bond order parameter $\Psi_{6,j}$ of two molecules separated by an in-layer distance r , and is given by,^{17,20}

$$G_{6,j}(r) = \langle \Psi_{6,j}^*(0) \Psi_{6,j}(r) \rangle. \quad (4)$$

For the case of $D^* = 5.5$ and 7.5 , we monitored $\Phi_{6,j}$, $g_j(r)$, and $G_{6,j}(r)$ for all the layers except the innermost (a highly localized quasirow of particles at the center of the pore), for which we monitored the local density of adsorbate ρ_{inner}^* . For the case of $D^* = 9.7$, we measured $\Phi_{6,j}$, $g_j(r)$, and $G_{6,j}(r)$ for the three outer layers (contact, second, and third). The fourth and innermost layers were considered together since we already showed that they behave similarly upon freezing.²⁶ In order to get information about the structure of the adsorbate in these inner regions of the pore, we used the 3D bond orientational order parameters proposed by Steinhardt *et al.*,³⁹

$$Q_l = \left[\frac{4\pi}{2l+1} \sum_{m=-l}^l |\bar{Q}_{lm}|^2 \right]^{1/2}, \quad (5)$$

$$W_l = \frac{1}{\left(\sum_{m=-l}^l |\bar{Q}_{lm}|^2 \right)^{3/2}} \sum_{m_1, m_2 = -l}^l \begin{pmatrix} l & l & l \\ m_1 & m_2 & -m_1 - m_2 \end{pmatrix} \times \bar{Q}_{lm_1} \bar{Q}_{lm_2} \bar{Q}_{l(-m_1 - m_2)}, \quad (6)$$

$$\bar{Q}_{lm} = \frac{1}{N_b} \sum_{i=1}^{N_b} Y_{lm}(\theta_i, \varphi_i), \quad (7)$$

where θ_i and φ_i are the polar and azimuthal angles giving the orientation of a given nearest-neighbor bond, Y_{lm} are spherical harmonics,⁴⁰ and the matrix in Eq. (6) is a representation

TABLE I. Values of the 3D bond orientational order parameters for some common 3D crystals. Taken from Ref. 16.

Crystal	Q_6	Q_4	W_6	W_4
fcc	0.571	0.191	-0.013	-0.159
hcp	0.485	0.097	-0.012	0.134
bcc	0.511	0.036	0.013	0.159
sc	0.354	0.764	0.013	0.159
Icosahedral	0.663	0	-0.170	0
Liquid	0	0	0	0

of the Wigner $3J$ symbols.⁴¹ We followed previous studies^{24,38} in choosing Q_6 to monitor the freezing behavior in the inner regions of the adsorbate; we also measured Q_4 , W_6 , and W_4 , finding consistent agreement between the behavior of the four parameters with temperature. Values of these 3D bond orientational order parameters for some common crystals are presented in Table I.

To further analyze the structure and the freezing behavior of the adsorbate in the inner regions ($D^*=9.7$), we generated a “renormalized” 3D positional pair-correlation function $g(R)$, given by,^{42–44}

$$g(R) = \frac{g_R(R)}{g_u(R)}, \quad (8)$$

where R represents the 3D distance between molecules in the fourth and innermost layers, $g_R(R)$ is given by the regular 3D radial distribution function, and $g_u(R)$ is the “uniform fluid” pair-correlation function. The latter only depends on geometry, and it is a correction due to excluded volume effects.⁴² In this particular case, $g_u(R)$ measures the number of pairs separated by a distance R that can be fitted within the cylindrical volume defined by the adsorbate in the inner regions. In addition, to analyze the 3D structure of the confined adsorbate at different temperatures, we measured the renormalized pair-correlation function $g(R)$ for all the adsorbate molecules for the three pore diameters considered. The procedure to estimate $g_u(R)$ for this case is similar, the only difference being that the complete pore volume ($D^*=9.7$, 7.5, and 5.5) was considered since the space outside the carbon nanotube was inaccessible to the molecules.

The average properties of the confined phase (amount adsorbed, local-density profile in the radial direction, and average order parameters in each layer/region) were determined using the PT-GCMC technique. On the other hand, the in-plane positional and orientational pair-correlation functions $g_j(r)$ and $G_{6,j}(r)$, and the “renormalized” 3D positional pair-correlation function $g(R)$ were determined from standard GCMC simulations, using the final configurations from parallel tempering as initial configurations for the conditions of interest.

D. Free-energy calculations

Although the use of the parallel tempering technique in simulations greatly reduces the probability of getting trapped in a metastable state, a free-energy calculation is required to rigorously determine the thermodynamic stability of each phase, as well as to unambiguously establish the values of

the thermodynamic transition temperatures. For the case of $D^*=9.7$ we determined the Landau free-energy^{17,45,46} Λ of the adsorbate at different temperatures:

$$\Lambda = -k_B T \ln[P(\Phi_i)] + \text{const}, \quad (9)$$

where $P(\Phi_i)$ is the probability distribution function of observing the system having a certain value of a spatially varying order parameter Φ_i . For the case of LJ CCl_4 freezing within a MWCNT with $D^*=9.7$, for which there are five layers of adsorbate, the Landau free energy can be expressed as

$$\Lambda = -k_B T \ln[P(\Phi_{6,\text{contact}}; \Phi_{6,\text{second}}; \Phi_{6,\text{third}}; Q_{6,\text{inner}})] + \text{const}. \quad (10)$$

The probability distribution function $P(\Phi_{6,\text{contact}}; \Phi_{6,\text{second}}; \Phi_{6,\text{third}}; Q_{6,\text{inner}})$ is calculated during a simulation run by collecting statistics of the number of occurrences of combinations of values for these order parameters in a four-dimensional histogram. To collect the statistics, we have combined GCMC simulations and umbrella sampling in partially overlapping windows of an order parameter^{16,17,46} with the parallel tempering technique³³ to improve sampling. In essence, the procedure is very similar to that described in Refs. 17 and 46, with some variations to incorporate the parallel tempering scheme. The 2D order parameter of the contact layer, $\Phi_{6,\text{contact}}$ was chosen to be the principal coordinate^{17,46} for the umbrella sampling procedure, since the adsorbate close to the pore walls is the first to freeze for the case of strongly attractive cylindrical pores.^{22–27} The possible range of values of $\Phi_{6,\text{contact}}$ was divided into 20 windows, which were found to be enough to ensure the collection of relevant statistics. Starting from well-equilibrated liquid phases, we performed a normal PT-GCMC simulation run with 16 replicas, constraining the order parameter $\Phi_{6,\text{contact}}$ to be within the range of the first window for all the replicas. During such a simulation, the other three order parameters were not constrained, and the probability distribution function P was calculated for that range of $\Phi_{6,\text{contact}}$. After finishing this run, we took the configurations corresponding to the maximum value of $\Phi_{6,\text{contact}}$ in the first window, and used them to start the simulations for the second window, which partially overlapped the range of values of $\Phi_{6,\text{contact}}$ of the first window. This procedure was repeated until we sampled the complete range of possible values of $\Phi_{6,\text{contact}}$. A typical run in each window involved averaging thermodynamic properties over at least 1500 million MC steps.

From this first set of runs we obtained 20 individual pieces of the four-dimensional probability distribution function $P(\Phi_{6,\text{contact}}; \Phi_{6,\text{second}}; \Phi_{6,\text{third}}; Q_{6,\text{inner}})$, which can be put together to obtain a continuous function, and obtain the Landau free energies from (10). We could not follow the procedure described in Ref. 46 to join the different pieces of Λ , since the probability P was very close to zero for some regions of phase space, causing Λ to take unphysical high values [see (10)]. This situation corresponded to very improbable or even unphysical configurations, e.g., one in which the contact layer is liquid, the second is solid, the third is liquid,

and the inner regions solid. In order to obtain nonzero values of probability for all possible combinations of our four order parameters, one would need to divide all their possible values in a number of windows, perform simulations constraining these four order parameters to be within the range of each window, and repeat this until all possible combinations of the order parameters would be covered. This would require a prohibitive number of simulations (e.g., if each order parameter range is divided in ten windows, such a procedure will require 10^4 simulations!).

To overcome these problems, we decided to put together the individual pieces of $P(\Phi_{6,\text{contact}}; \Phi_{6,\text{second}}; \Phi_{6,\text{third}}; Q_{6,\text{inner}})$ by adding suitable constants, equal to the average of the differences between probability values found in the overlapping region between adjacent windows of $\Phi_{6,\text{contact}}$. This procedure was implemented in the same spirit as the combination of histograms using histogram reweighting techniques.⁴⁷ After such procedure, we normalized the entire probability distribution function P . In this way, we obtain a single probability distribution hypersurface that is continuous in all the four dimensions, and the values of the four order parameters that correspond to global and local maxima in P (and minima in Λ) can be accurately determined. We do not expect the location of such maxima in P to be altered by the procedure to put together the individual pieces of P . Those free-energy minima can also be compared with PT-GCMC results, providing further assessment of both series of simulations. On the other hand, we are unable to draw conclusions about the accuracy of the free-energy barriers between stable and metastable states. Such barriers are subject to strong finite-size effects,^{17,38,46} and they are not the main objective of our investigation.

Following this procedure, we obtained a first estimate of the probability distribution function $P(\Phi_{6,\text{contact}}; \Phi_{6,\text{second}}; \Phi_{6,\text{third}}; Q_{6,\text{inner}})$, by sampling the most important regions of the phase space defined by the four order parameters selected, and without using any weighting function in the umbrella sampling. To further refine the calculation of the probability distribution function, the procedure outlined above was repeated using a weighting function w , in addition to the usual acceptance criteria for parallel tempering GCMC simulations. The weighting function chosen in this case was equal to $w(\Phi_{6,\text{contact}}) = 1/P^{(1)}(\Phi_{6,\text{contact}})$, where $P^{(1)}(\Phi_{6,\text{contact}})$ was calculated by numerically integrating P with respect to all the order parameters except $\Phi_{6,\text{contact}}$. The numerical integration was done using the Simpson's rule.⁴⁸ It was reported in previous studies^{16,38,46} that successive iterations with such a procedure increase the accuracy of the distribution functions, but just one iteration is usually needed to achieve convergence. In this sense, the use of a single order parameter ($Q_{6,\text{inner}}$), rather than two ($\Phi_{6,\text{outer}}$ and $\Phi_{6,\text{inner}}$), to characterize the degree of order in the inner regions of the pore, reduces the dimensionality of the probability distribution P and facilitates sampling of phase space.

The grand free energy of the phases, $\Omega = -k_B T \ln \Xi$ (where Ξ is the grand partition function), is related to the probability distribution function (and thus to the Landau free energy) by,^{16,17}

$$\begin{aligned} \exp(-\beta\Omega) &= \int d\Phi_{6,\text{contact}} \int d\Phi_{6,\text{second}} \int d\Phi_{6,\text{third}} \\ &\times \int dQ_{6,\text{inner}} \\ &\times P[\Phi_{6,\text{contact}}; \Phi_{6,\text{second}}; \Phi_{6,\text{third}}; Q_{6,\text{inner}}], \end{aligned} \quad (11)$$

where $\beta = 1/k_B T$. To calculate the grand free energy of a phase, the integration in (11) is done from the minimum to the maximum values of the four order parameters that characterize the phase. The previous calculation determines the grand free-energy difference between the phases at a particular value of temperature and chemical potential. To relate the grand free energy of a particular phase at two different values of T and μ , we numerically integrate the following equations:^{16,49}

$$\left[\frac{\partial \Omega}{\partial \mu} \right]_{T,V} = -N, \quad (12)$$

$$\left[\frac{\partial(\Omega/T)}{\partial(1/T)} \right]_{\mu,V} = U - N\mu, \quad (13)$$

where U and N are the total internal energy and number of molecules of the system, respectively. The thermodynamic transition temperatures and the order of the transitions can be determined from these calculations.

III. RESULTS

A. $D^* = 9.7$ pore

PT-GCMC simulations were performed for LJ CCl_4 within a structureless model MWCNT of $D^* = 9.7$ ($D = 5$ nm). In Fig. 2 we report the average values of the bond order parameters as a function of temperature. The 2D order parameters $\Phi_{6,j}$ were measured for the three layers close to the walls (contact, second, and third), whereas the 3D order parameter $Q_{6,\text{inner}}$ was determined for the adsorbate in the center of the pore (fourth and innermost layers). The behavior in the contact and second layers is very similar: a steep increase in $\Phi_{6,j}$ around 250–260 K, followed by slight increases in $\Phi_{6,j}$ with further reduction of the temperature. These results suggest that both molecular layers undergo a transition from isotropic liquid ($\Phi_{6,j} \sim 0.1$, due to finite-size effects) to a defective quasi-2D hexagonal crystal ($\Phi_{6,j} \sim 0.8$) at temperatures around 260 K, which are slightly higher than the bulk freezing point of LJ CCl_4 (251 K). The change in $\Phi_{6,j}$ for the third layer is more gradual than for the first two layers and occurs over a wider temperature range, around 220–260 K. The adsorbate in the center of the pore shows gradual increases in $Q_{6,\text{inner}}$ in the range 220–260 K, followed by a rise between 220 and 190 K, reaching a value of ~ 0.30 at $T = 177$ K. In a previous study,²⁶ rather than $Q_{6,\text{inner}}$ we measured the 2D order parameters $\Phi_{6,j}$ for the fourth and innermost layers, and we found a similar behavior as the temperature was reduced. This indicates that $Q_{6,\text{inner}}$, as well as

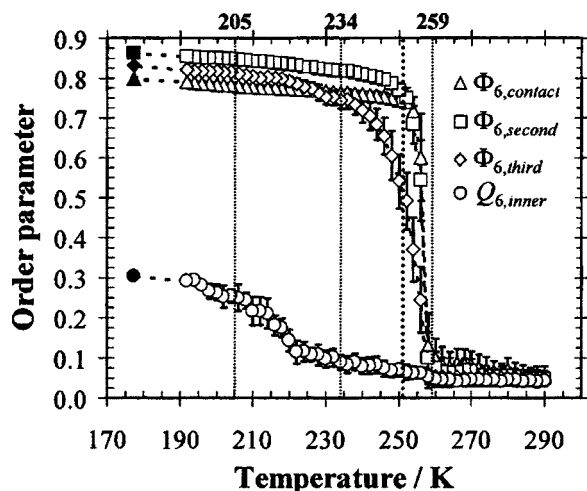


FIG. 2. Average values of the bond order parameters measured for LJ CCl_4 confined in a structureless MWCNT with $D^* = 9.7$, as a function of temperature. $\Phi_{6,j}$ was measured for the contact, second, and third layers, and $Q_{6,\text{inner}}$ is reported for the adsorbate in the center of the pore (fourth and innermost layers). The black-filled symbols represent the results from a GCMC simulation performed at $T = 177$ K. The thick-dotted line represents the bulk melting point of LJ CCl_4 (251 K). The three thin-dotted lines represent the experimental transition temperatures (205, 234, and 259 K) of CCl_4 within MWCNT with $D = 5$ nm, from dielectric relaxation spectroscopy measurements (see Refs. 26 and 27).

$\Phi_{6,\text{inner}}$ and $\Phi_{6,\text{fourth}}$, are equivalent and suitable order parameters to detect freezing of adsorbate in the inner regions, at least for this particular pore size.

The difference in the temperature ranges at which each layer undergoes a transition from an isotropic phase to an ordered structure can be explained in terms of a competition between attractive interactions and degree of confinement; strongly attractive walls lead to increases in the adsorbate transition temperatures, whereas geometrical constraints produce depressions in the transition temperatures. The contact layer experiences a strong attraction from the pore wall, and the combined interaction of the pore wall and the contact layer acts upon the second layer. Consequently, these two layers undergo a transition at temperatures slightly higher than the bulk freezing point. In contrast, the fourth and innermost layers experience a weaker effect from the attractive wall potential and are the most geometrically constrained; therefore, the liquid-solid transition occurs at temperatures well below the bulk freezing point, and the ordered phase presents a large number of defects. Finally, the third layer undergoes a transition at intermediate temperatures, since its geometrical constraint is not as severe as in the inner regions and the effect of the pore walls is weaker than in the outer layers. As already discussed elsewhere,^{26,27} our simulation results are consistent with the experimental transition temperatures measured using dielectric relaxation spectroscopy for the same system: 259 K should represent the end of melting in the outer layers of adsorbate, whereas 205 and 234 K should represent the beginning and end of the melting process in the inner regions of the pore.

Results for the 2D positional and bond orientational pair-correlation functions $g_j(r)$ and $G_{6,j}(r)$ are shown in Fig. 3, for the first three layers of CCl_4 within the MWCNT with $D^* = 9.7$. We also report in this figure the 3D positional

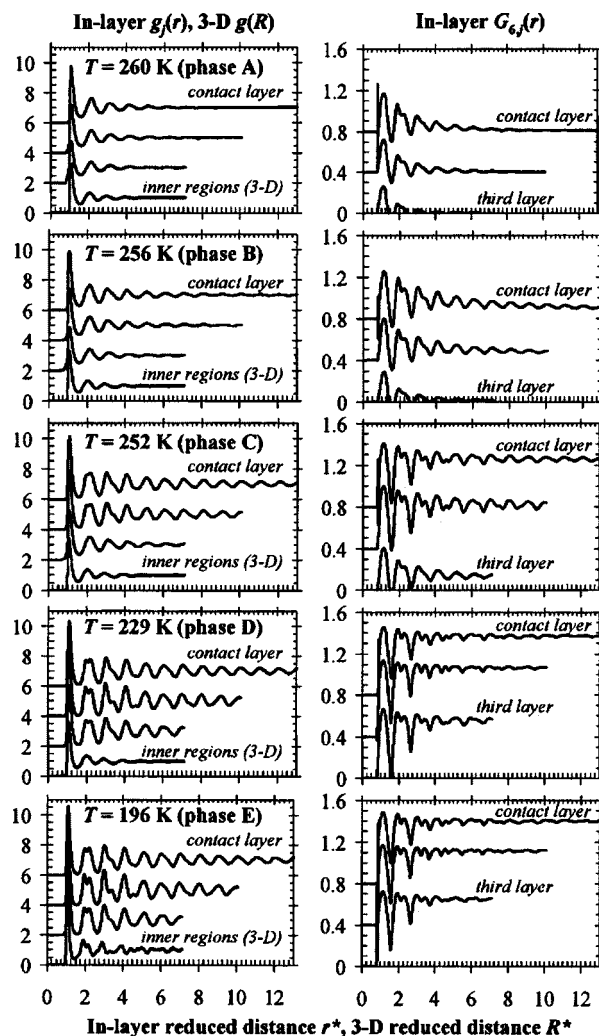


FIG. 3. 2D positional and bond orientational correlation functions, $g_j(r)$ and $G_{6,j}(r)$, for the first three molecular layers of adsorbate, and 3D positional correlation function corrected by excluded volume effects, $g(R)$, for the adsorbate in the center of the pore. Five different confined phases A, B, C, D, and E (see text for descriptions) can be observed for LJ CCl_4 within a structureless MWCNT of $D^* = 9.7$ at different temperatures. For clarity, the $g_j(r)$ functions corresponding to the contact, second, and third layers have been shifted by +6, +4, and +2, respectively. In a similar way, the $G_{6,j}(r)$ functions corresponding to the contact and second layers have been displaced by +0.8 and +0.4, respectively.

correlation function $g(R)$ for the inner regions (fourth and innermost layers), which has been corrected for excluded volume effects.^{42–44} Correlations in each layer were reported in these figures up to a distance $l = \pi r_l$, where r_l is the radial position where the reduced local-density ρ^* reaches a maximum in each layer [see Fig. 1(a)]; correlations in the inner regions were arbitrarily reported up to $l \sim 7.25\sigma_{ff}$, the value of l corresponding to the third layer. At $T = 260$ K, $g_j(r)$ and $g(R)$ exhibit liquidlike features and $G_{6,j}(r)$ decays exponentially. Therefore, all adsorbate regions behave as dense liquids (no crystalline order) with short-range positional and bond orientational order (phase A). At $T = 256$ K, the contact and second layers have an intermediate morphology between a quasi-2D hexagonal crystal and a liquid, while the rest of the adsorbate presents a liquidlike structure (phase B). The $g_j(r)$ for the contact and second layers shows liquidlike features with extended correlations, as compared to the $g_j(r)$ at

260 K. In addition, the $G_{6,j}(r)$ for these two layers decays at a slower rate, as compared to the $G_{6,j}(r)$ at 260 K; moreover, $\Phi_{6,j}$ for these two layers (Fig. 2) takes intermediate values between those exhibited by a liquid ($\Phi_{6,j} \sim 0.1$) and a quasi-2D crystal ($\Phi_{6,j} \sim 0.8$). This 2D phase for the contact and second layers resembles a hexatic phase, which is expected in the framework of the KTHNY theory for 2D melting.^{19–21} This theory involves two continuous transitions: first, between a 2D crystal phase (with quasilong-range positional order and long-range bond orientational order) and a hexatic phase (with positional disorder and quasilong-range bond orientational order); and second, between the hexatic phase and the 2D liquid phase (with positional and bond orientational disorder). System size is a key variable in rigorously determining the nature of intermediate phases between 2D crystals and liquids.^{17,18} A rigorous system size scaling analysis, which has been done for LJ fluids within slit pores to determine the existence of hexatic phases,¹⁸ cannot be performed for cylindrical pores of a few nanometers since the dimensions of the quasi-2D layers of adsorbate are limited by the pore diameter. In consequence, the intermediate phases observed in the contact and second layers at 256 K cannot be rigorously termed hexatic phases; however, they exhibit remnants of hexatic behavior.

At $T=252$ K, both the contact and second layers appear as quasi-2D hexagonal crystals with defects; the third layer exhibits an intermediate morphology similar to that observed for the first two layers at 256 K, and the center of the pore keeps its isotropic characteristics (phase C). The crystalline nature of both contact and second layers is determined from the features observed in the $g_j(r)$ functions: a large value on the first peak, a first minimum of zero, and an incipient splitting in the second and third peaks. The constant value of $G_{6,j}(r)$ at relatively large r for the two outer layers is also a signature of phases having long-range bond orientational order. At $T=229$ K, the third layer exhibits the same crystalline features as the outer layers, while the inner regions are still liquidlike (phase D). Finally, all the adsorbates have quasicrystalline morphology at $T=196$ K (phase E). CCl_4 in the inner regions suffers strong geometrical constraints and consists of frustrated crystals with a large number of defects, as evidenced by the nonzero first minimum in $g(R)$. The temperature must reach values as low as $T=196$ K to observe nonisotropic features for $g(R)$ in the inner regions of the pore.

In order to rigorously determine the thermodynamic stability of each phase, we measured the probability distribution function $P(\Phi_{6,\text{contact}}; \Phi_{6,\text{second}}; \Phi_{6,\text{third}}; Q_{6,\text{inner}})$ for the case of LJ CCl_4 within a MWCNT of reduced diameter $D^*=9.7$. We used the methodology described in Sec. II D to measure such probabilities at different sets of (T, μ) . In Fig. 4 we present the first-order distribution functions of the probability, $P^{(1)}$, for the four order parameters at a representative temperature, $T=252$ K. The first-order distribution $P^{(1)}$ is obtained by integrating $P(\Phi_{6,\text{contact}}; \Phi_{6,\text{second}}; \Phi_{6,\text{third}}; Q_{6,\text{inner}})$ with respect to all the order parameters except one [e.g., $P^{(1)}(\Phi_{6,\text{contact}})$ was obtained by integrating P with respect to all the order parameters except $\Phi_{6,\text{contact}}$; the same principle applies to $P^{(1)}(\Phi_{6,\text{second}})$, $P^{(1)}(\Phi_{6,\text{third}})$, and $P^{(1)}(Q_{6,\text{inner}})$]. The four $P^{(1)}$

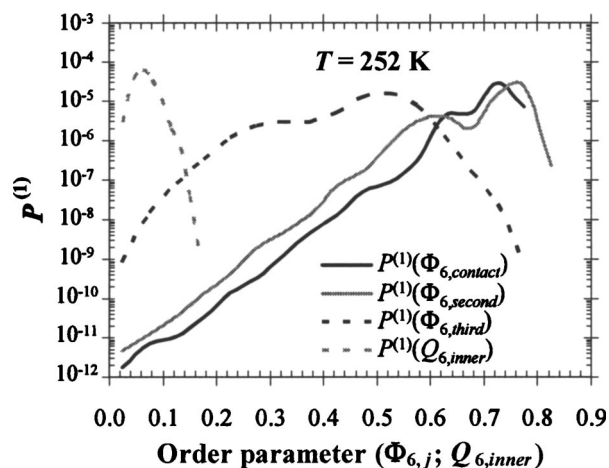


FIG. 4. First-order distribution functions of the probability $P(\Phi_{6,\text{contact}}; \Phi_{6,\text{second}}; \Phi_{6,\text{third}}; Q_{6,\text{inner}})$ for LJ CCl_4 within a structureless MWCNT of $D^*=9.7$ at $T=252$ K. The distribution function $P^{(1)}(\Phi_{6,\text{contact}})$ was obtained by numerically integrating P with respect to all the order parameters except $\Phi_{6,\text{contact}}$; the same principle applies to $P^{(1)}(\Phi_{6,\text{second}})$, $P^{(1)}(\Phi_{6,\text{third}})$, and $P^{(1)}(Q_{6,\text{inner}})$.

curves span over a wide range of order parameter values, showing that the simulations were able to sample a wide range of phase space. The four global maxima in each of the $P^{(1)}$ functions represent maxima in the total probability distribution function P . Since the Landau free-energy Λ is related to the probability P through (10), the combination of the four maxima in $P^{(1)}$ gives the equilibrium configuration within the pore at a given temperature. From Fig. 4, it can be seen that phase C (contact and second layers as quasi-2D hexagonal crystals with defects, third layer with intermediate morphology between 2D liquid and crystal, and inner regions still liquidlike) is the most stable phase at $T=252$ K, in agreement with the results from PT-GCMC simulations (Figs. 2 and 3). Similar agreement was found for all the temperatures considered in the free-energy calculations. This comparison shows that the PT-GCMC simulations are capable of giving results which are at least very close to true equilibrium results, provided that the fraction of accepted swap moves is high enough. For $D^*=9.7$, such fraction was 30% for the worst case, i.e., between replicas with temperatures around the transition points for the outer layers of adsorbate.

The grand free-energy Ω of the different phases (A–E) can be determined from the probability distribution function $P(\Phi_{6,\text{contact}}; \Phi_{6,\text{second}}; \Phi_{6,\text{third}}; Q_{6,\text{inner}})$ by using Eqs. (11)–(13). Plots of the grand free-energy Ω of the different phases as a function of the temperature T near the transition points are shown in Fig. 5. To facilitate visualization, in each plot we present the difference of grand free energy of each phase with respect to phase A. The most stable phase in each temperature range is the one with the lowest grand free energy, and the intersection between the curves gives us the thermodynamic transition temperatures. The transitions between phases A–B, B–C, and C–D occur at $T=256.5$ K, $T=254.0$ K, and $T=248.2$ K, and they are first order (the grand free energy curves intersect with different slopes). These phase transitions involve freezing in the contact, second, and third layers of adsorbate. Rather than going directly

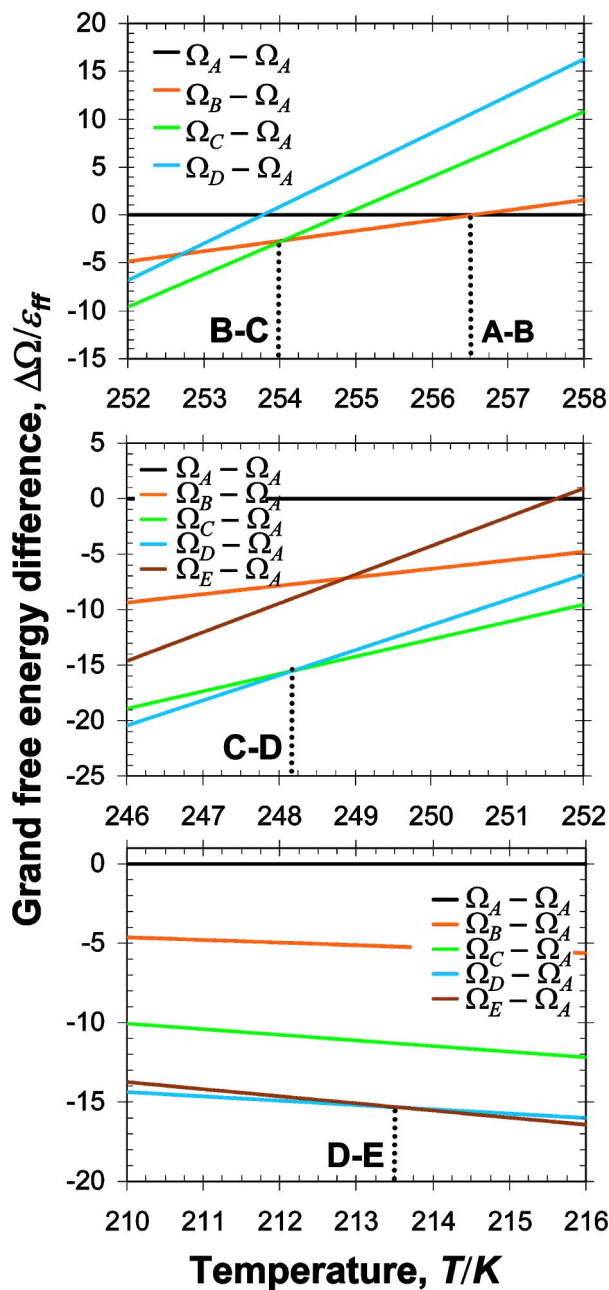


FIG. 5. Grand free-energy Ω of the different phases as a function of temperature T , for LJ CCl_4 confined within a structureless MWCNT of $D^* = 9.7$. To facilitate visualization, the difference of grand free energy of each phase with respect to phase A is presented, and three plots are provided for temperature ranges close to the transition points.

from quasi-2D isotropic liquid to quasi-2D hexagonal crystals, freezing in these layers occurs via intermediate phases that show remnants of hexatic behavior. According to the KTHNY mechanism of freezing/melting, in a true 2D system the transitions liquid-hexatic and hexatic-crystal are of continuous nature.¹⁹⁻²¹ Nevertheless, for quasi-2D systems, e.g., LJ fluids confined within narrow slit pores accommodating several molecular layers,¹⁶⁻¹⁸ such transitions were found to be first order, due to the interaction between molecules in different layers. For LJ CCl_4 within a cylindrical pore, we have the effect of both interlayer interactions and pore curvature. The latter effect might cause phases B and C (which involve intermediate phases in the contact, second, and third

TABLE II. Thermodynamic transition temperatures and phases involved, for LJ CCl_4 confined within a MWCNT with $D^* = 9.7$, as determined from free-energy calculations. See text for descriptions of the different phases.

Transition temperatures	Phases involved
256.5	A-B
254.0	B-C
248.2	C-D
213.5	D-E

layers) to be stable over a relatively small range of temperatures (2.5 K for phase B, 5.8 K for phase C), as compared to what was observed for LJ CCl_4 within strongly attractive slit pores,¹⁷ where the hexatic phase was stable over a range of 57 K.

The transition between phases D and E takes place at $T = 213.5$ K, and it is of weaker first-order nature as compared to the transitions previously described. The transition temperature and its nature are difficult to establish in this case due to the very small difference in the slopes of Ω . This is in agreement with the results presented in Fig. 2, where the increase in $Q_{6,\text{inner}}$ is more gradual and occurs over a wider temperature range as compared to the contact, second, and third layers. The transition between phases D and E involves freezing in the inner regions of the pore, which evolve from liquidlike to frustrated crystal structures with defects due to geometrical constraints. It is reasonable to expect such a transition to be weakly first order, since the differences between these two phases are not very marked. It is important to note that transitions can be observed even in the narrow inner regions, where particles depart from a truly one-dimensional (1D) system behavior (with no phase transitions) because of the interactions with the neighboring molecular layers. Similarly, it has been shown⁵⁰ that particles forming a 1D system within a zeolite can undergo gas-liquid phase transitions at low temperatures due to pore-pore correlation effects.

The significant changes in the order parameter for the different phases further suggest that all the transitions observed are first order. The change of sign of the grand free-energy differences between the phases [i.e., $\Omega_A - \Omega_B > 0$ at the lowest values of (T, μ) , and $\Omega_A - \Omega_B < 0$ at the highest values of (T, μ)], also implies that the phase transitions are first order. All the transition points determined from the free-energy calculations are within the range of temperatures determined from the analysis of Figs. 2 and 3. The thermodynamic transition temperatures and the phases involved in each transition are summarized in Table II.

B. Smaller pore diameters: $D^* = 7.5$ and 5.5

PT-GCMC simulations were performed to study the freezing behavior of LJ CCl_4 confined within structureless MWCNT of diameters $D^* = 7.5$ and 5.5. We did not attempt to perform free-energy calculations for these pore diameters, since for $D^* = 9.7$ it was shown that PT-GCMC simulations give results very close to true equilibrium results.

The amount adsorbed as a function of temperature for $D^* = 7.5$ and 5.5 is presented in Fig. 6. For $D^* = 7.5$ [Fig.

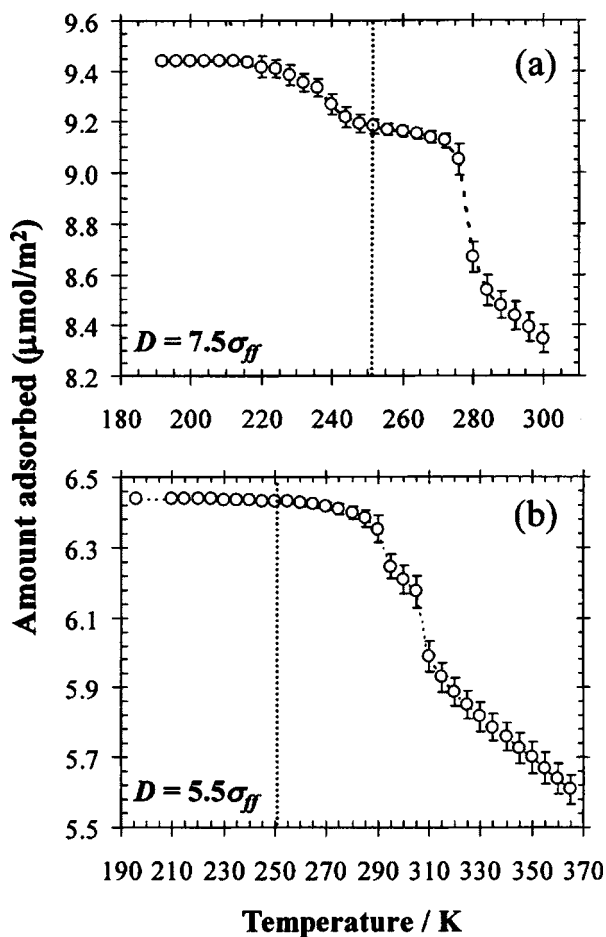


FIG. 6. Amount adsorbed as a function of temperature for LJ CCl_4 confined within a structureless MWCNT of (a) $D^* = 7.5$, and (b) $D^* = 5.5$. The thick-dotted line represents the bulk melting point of LJ CCl_4 for all cases.

6(a)], the quantity of adsorbate increases gradually as the temperature decreases, up to temperatures around 276–284 K, where a jump is observed. Further reduction in the temperature produces increases in the amount adsorbed within the MWCNT; the slope of the curve is higher for the range $216 \text{ K} < T < 248 \text{ K}$, as compared to that for $248 \text{ K} < T < 276 \text{ K}$. For $T < 216 \text{ K}$, further reduction of temperature produces negligible variations in the curve. Similarly, for $D^* = 5.5$ [Fig. 6(b)] the quantity of adsorbate increases gradually up to 305–310 K, when a steep rise in the curve is observed. The amount adsorbed increases again gradually until another small jump in the curve is seen at 290–295 K and finally reaches a plateau around 265 K.

In Fig. 7 we show the average 2D bond order parameters $\Phi_{6,j}$ as a function of temperature for the different layers of adsorbate, except the innermost (a highly localized quasirow of particles at the center of the pore), for which we monitored the local density of adsorbate ρ_{inner}^* . For $D^* = 7.5$, Fig. 7(a) shows steep jumps in the average order parameter values of the contact and second layers in the range 276–284 K. The increases in order parameter and local density are slightly more gradual for the third and innermost layers, respectively, and occur for $268 \text{ K} < T < 284 \text{ K}$. Analysis of snapshots from typical configurations indicate that, as the local density increases in the innermost layer with reduction

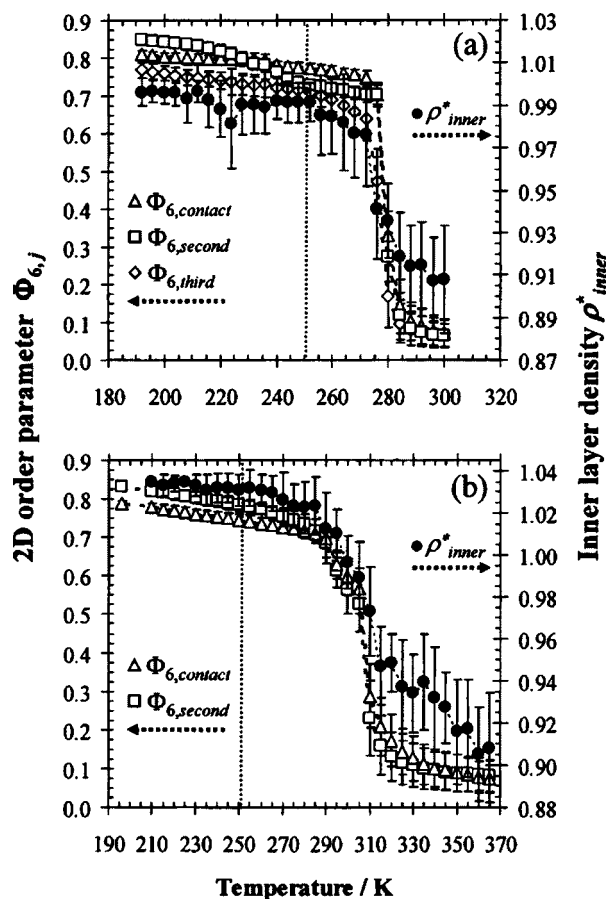


FIG. 7. Average values of the 2D bond order parameters $\Phi_{6,j}$ (open symbols, left ordinate axis), and reduced local density for the innermost layer ρ_{inner}^* (black-filled circles, right ordinate axis), as a function of temperature, for (a) $D^* = 7.5$, and (b) $D^* = 5.5$. The thick-dotted line represents the bulk melting point of LJ CCl_4 for all cases.

of temperature, molecules in this layer become more localized around the pore axis. Nevertheless, the innermost layer does not become a perfect 1D system even at the lowest temperature studied ($T = 192 \text{ K}$). By comparing Figs. 6(a) and 7(a), it can be established that the jump observed in the amount adsorbed around 276–284 K [Fig. 6(a)] is associated with freezing of the contact, second, and third layers of adsorbate, as well as with the increase in the local density of the innermost layer. All these changes occur at temperatures well above the bulk freezing point (251 K for LJ CCl_4). For temperatures between 216 and 248 K, the rate of increase of the average order parameter for the second layer [Fig. 7(a)] is slightly higher than those for the other layers, and therefore the features observed in the curve of amount adsorbed at $216 \text{ K} < T < 248 \text{ K}$ [Fig. 6(a)] can be associated with the increase of crystalline order in the second layer.

For $D^* = 5.5$ [Fig. 7(b)], steep increases in the 2D order parameter values are observed for both contact and second layers at 305–310 K; similarly, the local density for the innermost layer also increases in this temperature range. Therefore, the contact and second molecular layers freeze in this temperature range; similarly, molecules in the innermost layer become more localized around the pore axis around these temperatures, which are significantly higher than the bulk freezing point. All these changes lead to the steep rise in

the amount adsorbed at 305–310 K [Fig. 6(b)]. The small jump in the amount adsorbed around 290–295 K can be associated with a higher rate of increase of the order parameter for the second layer [Fig. 7(b)], as compared to that for the contact, as observed for $D^*=7.5$. Although the contact and second layers solidify simultaneously for all the pore sizes studied in this work, the average order parameter of the second layer is always higher than that of the contact layer at the lowest temperatures. This effect occurs due to packing considerations: for the three pore sizes, the dimensions of the unfolded second layer ($2\pi r_l L$, where r_l is the radial position where the reduced local-density ρ^* reaches a maximum in layer l , see Fig. 1) are commensurate with an integer number of molecules arranged in hexagonal symmetry, but this is not the case for the contact layer. As a result, molecules in the second layer can pack more efficiently than those in the contact layer, making the average order parameter and the in-plane density larger for the second layer. This finding is in agreement with the GCMC results of Kanda *et al.*,²³ who obtained a higher in-plane density for the second layer of adsorbate as compared to that of the contact layer. This effect is dependent on pore size: a small change in this variable can lead to a more efficient packing in the contact layer. Such an effect, which was not observed in slit pores,^{14,16,17} emphasizes the role of geometric constraints in the pores of cylindrical geometry. It is important to note again that transitions can be observed in the narrow inner regions of adsorbate within the MWCNT with $D^*=7.5$ and 5.5, since particles do not form a truly 1D system (for which phase transitions are not possible for $T>0$ K).

The structure of the confined phase within the MWCNT with $D^*=7.5$ and 5.5 can be determined from the analysis of the in-plane positional and bond orientational pair-correlation functions $g_j(r)$ and $G_{6,j}(r)$. For the case of $D^*=7.5$, at $T=282$ K the contact, second, and third layers have a liquidlike structure, and the innermost layer exhibits relatively low values of local density (structure A, similar to phase A for $D^*=9.7$, Fig. 3). The intermediate quasi-2D phases are seen again in the contact, second, and third layers at $T=280$ K, and ρ_{inner}^* starts to increase steeply (structure B). At this temperature, the contact, second, and third layers exhibit behaviors similar to what was observed for $D^*=9.7$ at $T=256$, 256, and 252 K, respectively (Fig. 3), i.e., extended correlations in $g_j(r)$ and $G_{6,j}(r)$ decay at a slower rate as compared to that observed at $T=282$ K. Also, the average order parameter of the contact, second, and third layers takes intermediate values between those of a quasi-2D liquid and a quasi-2D hexagonal crystal [see Fig. 7(a)]. At $T=270$ K, the contact, second, and third layers behave as quasi-2D hexagonal crystals with defects, and the innermost layer presents a relatively high value of ρ_{inner}^* (structure C, equivalent to phase D for $D^*=9.7$, Fig. 3). Further reduction of temperature only produces changes in packing, especially in the second molecular layer. It is important to mention that an intermediate structure between B and C may exist, where the contact and second layers behave as quasi-2D hexagonal crystals with defects and the third and innermost layers exhibit intermediate features (similar to phase C for $D^*=9.7$, Fig. 3). Nevertheless, it was difficult to observe such a struc-

TABLE III. Temperature range of each structure for LJ CCl_4 confined within MWCNT with $D^*=7.5$ and 5.5, as determined from PT-GCMC simulations. See text for descriptions of the different structures.

$D^*=7.5$		$D^*=5.5$	
Structure	Temperature range (K)	Structure	Temperature range (K)
A	$T \geq 282$	A	$T \geq 318$
B (*) ^a	$270 \leq T \leq 282$	B	$295 \leq T \leq 318$
C	$T \leq 270$	C	$T \leq 295$

^a(*) For $D^*=7.5$, an intermediate structure between B and C may exist, where the contact and second layers behave as quasi-2D hexagonal crystals with defects, and the third and innermost layer exhibit intermediate features. See text for further details.

ture since finite-size effects are very important, especially for the third layer where correlations were measured up to distances of only $3.5\sigma_{ff}$. The differences between the quasi-2D isotropic liquid, intermediate phases and hexagonal crystals for the third layer are very subtle; this is especially true for $270 \text{ K} < T < 280 \text{ K}$, where the differences in $g_j(r)$ and $G_{6,j}(r)$ are not large enough to precisely determine the transition points and unambiguously determine the nature of such phases.

In a similar way, structure A for $D^*=5.5$ (contact and second layers as quasi-2D liquids, innermost layer with low local density) was observed around 318 K. Structure B (intermediate phases for contact and second layers, ρ_{inner}^* starts to increase steeply) is observed at approximately 305 K, and at 290 K structure C (contact and second layers as quasi-2D hexagonal crystals with defects, ρ_{inner}^* exhibiting high values) is obtained. Again, further temperature reduction causes packing changes in the adsorbate layers, especially in the second molecular layer. The rate of increase of $\Phi_{6,j}$ and ρ_{inner}^* upon reduction of temperature is more gradual for $D^*=5.5$, as compared to what is observed for $D^*=7.5$. The temperature ranges at which each structure was observed for both $D^*=7.5$ and 5.5, as obtained from PT-GCMC simulations, are summarized in Table III.

We note that the freezing behavior of the contact and second layers of LJ CCl_4 is similar for the three pore diameters studied [Figs. 2, 7(a), and 7(b)]; in each case they solidify at the same temperature, above the bulk freezing point (251 K for LJ CCl_4). As the pore diameter is reduced, the shift in freezing temperature in these two layers increases: solidification occurs around 305–310 K for $D^*=5.5$, between 276 and 284 K for $D^*=7.5$, and at 250–260 K for $D^*=9.7$. This effect of the pore size has been observed in previous studies^{22–27} of strongly attractive pores with cylindrical geometry, and has been explained as follows: the adsorbate-wall attractive interaction becomes stronger as the pore diameter is reduced, leading to larger increases in the solidification temperatures of the molecular layers close to the walls. Similarly, the third molecular layer for $D^*=7.5$ and $D^*=9.7$ experiences a more gradual solidification process with temperature, which involves temperatures above the bulk freezing point ($268 \text{ K} < T < 284 \text{ K}$) for $D^*=7.5$; in contrast, for $D^*=9.7$ solidification of the third layer involves a much wider range of temperatures ($220 \text{ K} < T < 260 \text{ K}$), above and below the bulk freezing point.

All layers/regions of LJ CCl_4 confined within the model carbon nanotubes studied in this work were able to experience morphology changes upon reduction of temperature, including the highly constrained molecules in the center of the pores. This behavior is in agreement with previous results obtained for strongly attractive cylindrical pores.^{22,23,25-27} On the other hand, these findings for strongly attractive pores contrast with previous results obtained by Sliwinski-Bartkowiak *et al.*²⁴ for weakly attractive silica pores. The authors reported amorphous phases for pore sizes with $D < 15\sigma_{ff}$, with the contact layer exhibiting remnants of hexatic behavior without crystallization, even at very low temperatures. These differences suggest that the strength of the adsorbate-wall interaction can produce both shifts in the confined transition temperatures and changes in the adsorbate structure upon reduction of temperature.

In Fig. 8 we show the 3D positional pair-correlation function $g(R)$ for the whole adsorbate within the three pore diameters studied at different temperatures, corrected by excluded volume effects.⁴²⁻⁴⁴ Correlations were measured in this case up to $30\sigma_{ff}$ (half of the total pore length). This function is of particular importance since its Fourier transform can be directly compared with the structure factor measured from scattering experiments. For $D^*=9.7$, solidlike features in $g(R)$ start to arise at temperatures as high as $T=252$ K; such features reflect the solidification of the contact and second layers (see Fig. 3). As the temperature is reduced, the first minimum of $g(R)$ slightly decreases, the splitting in the second peak becomes more evident, and the maximum in all the peaks of $g(R)$ slightly increases. Similar findings were obtained for $D^*=7.5$ and $D^*=5.5$, with the solidlike features appearing at $T=280$ and 305 K, respectively. The features observed in $g(R)$ for the whole pore arise since the adsorbate solidifies into different structures in the radial and axial directions: molecules form concentric layers in the radial direction, and within each layer, the particles arrange themselves into quasi-2D hexagonal crystals with defects. For distances less than the pore diameter [$R/\sigma_{ff} < 9.7$, Fig. 8(a); $R/\sigma_{ff} < 7.5$, Fig. 8(b); and $R/\sigma_{ff} < 5.5$, Fig. 8(c)], $g(R)$ for the whole pore includes characteristics from both structures (in radial and axial directions), and for larger distances the $g(R)$ features mainly reflect the quasi-2D hexagonal crystal morphology. In addition, the features of $g(R)$ for the whole pore indirectly reflect the fact that the different layers of adsorbate solidify at different temperatures.

IV. SUMMARY AND CONCLUSIONS

We have presented simulation results for freezing and melting of Lennard-Jones carbon tetrachloride confined within model multiwalled carbon nanotubes of different diameters. The structure and thermodynamic stability of the confined phases, as well as the temperatures and the order of the phase transitions, were determined from parallel tempering grand canonical Monte Carlo simulations and free-energy calculations using spatially inhomogeneous order parameters. The latter confirms that PT-GCMC simulations give equilibrium results, or at least very close to equilibrium. The simulations show that the adsorbate forms concentric

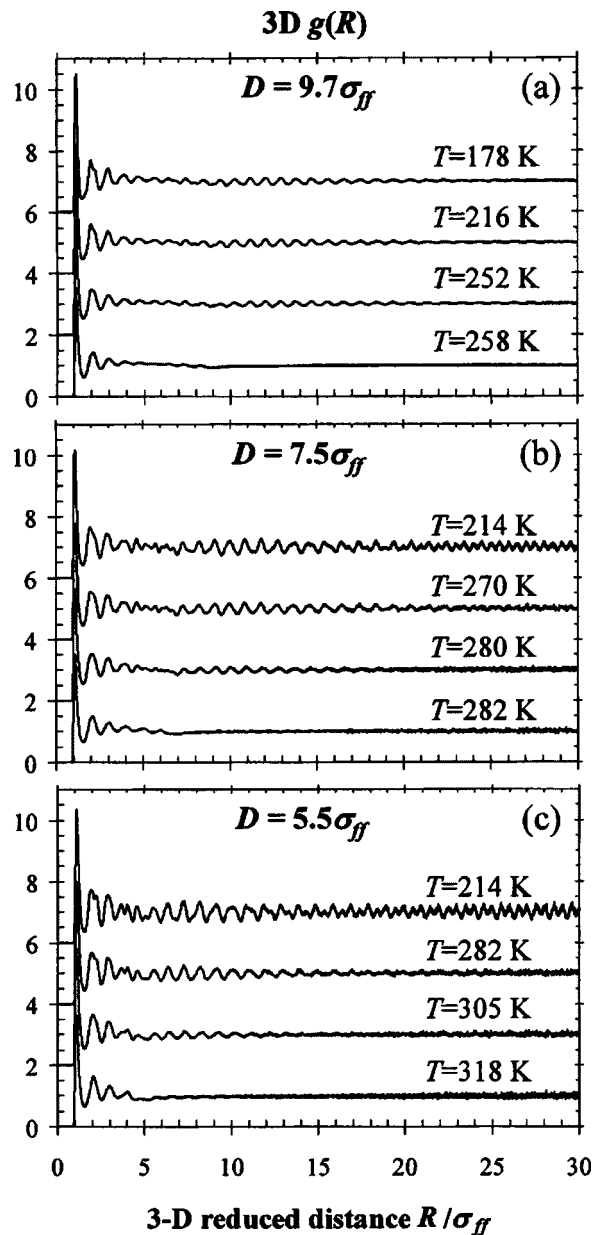


FIG. 8. 3D positional correlation function $g(R)$, corrected by excluded volume effects, for all the molecules of LJ CCl_4 confined within structureless MWNT: (a) $D^*=9.7$, (b) $D^*=7.5$, and (c) $D^*=5.5$, at different temperatures. Statistical noise can be observed for $g(R)$ at larger values of R/σ_{ff} , especially for the smaller pore diameters since the number of molecules separated by a distance R/σ_{ff} decreases as such distance becomes larger.

molecular layers that solidify into quasi-2D hexagonal crystals with defects. Freezing in such concentric layers occur via intermediate phases that show remnants of hexatic behavior, in a similar way to the freezing mechanism previously described for Lennard-Jones particles confined within slit pores.¹⁶⁻¹⁸ The transitions in these layers occur at temperatures that can be above or below the bulk freezing point, depending on the pore diameter and distance to the pore wall. Due to strong geometrical constraints, the adsorbate in the inner regions of the pore can either solidify into frustrated crystals with a large number of defects at temperatures well below the bulk freezing point ($D^*=9.7$), or molecules can form a highly localized row of particles at the center of the pore, exhibiting increases in the local density ρ_{inner}^* at

temperatures above the bulk freezing point ($D^*=7.5$ and 5.5). The simulations show evidence of a rich phase behavior in confinement. Five different phases were observed for the largest pore diameter studied ($D^*=9.7$), whereas three different structures were found for the other two pore sizes examined ($D^*=7.5$ and 5.5). Some of these phases were found to be inhomogeneous (i.e., combinations of crystalline, liquid, and frustrated crystalline regions) and stable over extended temperature ranges.

Further experiments with different techniques are needed to corroborate our observations. In previous works,^{26,27} we showed that the multiple transition temperatures observed in the simulations for CCl_4 within a MWCNT of $D=9.7\sigma_{ff}=5$ nm were consistent with the experimental transition temperatures from dielectric relaxation spectroscopy measurements. Experimental techniques such as nuclear magnetic resonance (NMR), x-ray diffraction, and neutron scattering would allow us to determine the structure of the confined adsorbate. From the simulation viewpoint, our future work will focus on how freezing in confinement is affected by the pore shape, surface roughness, and chemical heterogeneity, in addition to the ratio of the pore-adsorbate to the adsorbate-adsorbate interactions.⁵¹ It would also be interesting to determine the effect of bulk pressure on freezing in cylindrical pores, which has been studied in the past for slit pores.⁵² In addition, it will be of interest to study the possibility of solid-solid transformations within each layer of adsorbate upon changes on the diameter of the cylindrical pore, in direct analogy with previous studies in slit pore geometries.⁵³⁻⁵⁶

ACKNOWLEDGMENTS

This work was supported by grants from the National Science Foundation (Grant No. CTS-0211792) and the Committee of Scientific Research of Poland (Grant No. KBN 2P03B 014 24). International cooperation was possible, thanks to a NATO Collaborative Linkage Grant (Grant No. PST.CLG.978802). This research used supercomputing resources from the National Partnership for Advanced Computational Infrastructure (NSF/NRAC Grant No. MCA93SO11), the National Energy Research Scientific Computing Center (DOE Grant No. DE-FGO2-98ER14847), and the High Performance Computing Center at North Carolina State University. We are grateful to Henry Bock (North Carolina State University), Coray M. Colina (University of North Carolina at Chapel Hill), Ravi Radhakrishnan (University of Pennsylvania), and Martin Schoen (Technische Universität Berlin) for helpful discussions.

¹L. D. Gelb, K. E. Gubbins, R. Radhakrishnan, and M. Sliwinski-Bartkowiak, Rep. Prog. Phys. **62**, 1573 (1999).

²H. K. Christenson, J. Phys.: Condens. Matter **13**, R95 (2001).

³C. Alba-Simionesco, B. Coasne, K. E. Gubbins, R. Radhakrishnan, and M. Sliwinski-Bartkowiak, J. Phys.: Condens. Matter (submitted).

⁴J. Klein and E. Kumacheva, Science **269**, 816 (1995); J. Chem. Phys. **108**, 6996 (1998); **108**, 7010 (1998).

⁵U. Raviv, P. Laurat, and J. Klein, Nature (London) **413**, 51 (2001).

⁶U. Raviv, S. Giasson, J. Frey, and J. Klein, J. Phys.: Condens. Matter **14**, 9275 (2002).

⁷M. Sliwinski-Bartkowiak, G. Dudziak, R. Sikorski, R. Gras, K. E. Gubbins, and R. Radhakrishnan, Phys. Chem. Chem. Phys. **3**, 1179 (2001).

⁸F. Mugele, B. Persson, S. Zilberman, A. Nitzan, and M. Salmeron, Tribol.

Lett. **12**, 123 (2002).

⁹K. Kaneko, A. Watanabe, T. Iiyama, R. Radhakrishnan, and K. E. Gubbins, J. Phys. Chem. B **103**, 7061 (1999).

¹⁰A. Watanabe and K. Kaneko, Chem. Phys. Lett. **305**, 71 (1999).

¹¹M. Sliwinski-Bartkowiak, R. Radhakrishnan, and K. E. Gubbins, Mol. Simul. **27**, 323 (2001).

¹²M. Miyahara, M. Sakamoto, H. Kanda, and K. Higashitani, Stud. Surf. Sci. Catal. **144**, 411 (2002).

¹³R. Radhakrishnan, K. E. Gubbins, and M. Sliwinski-Bartkowiak, J. Chem. Phys. **112**, 11048 (2000).

¹⁴M. Miyahara and K. E. Gubbins, J. Chem. Phys. **106**, 2865 (1997).

¹⁵H. Dominguez, M. P. Allen, and R. Evans, Mol. Phys. **96**, 209 (1998).

¹⁶R. Radhakrishnan and K. E. Gubbins, Mol. Phys. **96**, 1249 (1999).

¹⁷R. Radhakrishnan, K. E. Gubbins, and M. Sliwinski-Bartkowiak, J. Chem. Phys. **116**, 1147 (2002).

¹⁸R. Radhakrishnan, K. E. Gubbins, and M. Sliwinski-Bartkowiak, Phys. Rev. Lett. **89**, 076101 (2002).

¹⁹For a review, see K. J. Strandburg, Rev. Mod. Phys. **60**, 161 (1988).

²⁰B. I. Halperin and D. R. Nelson, Phys. Rev. Lett. **41**, 121 (1978); D. R. Nelson and B. I. Halperin, Phys. Rev. B **19**, 2457 (1979).

²¹A. P. Young, Phys. Rev. B **19**, 1855 (1979).

²²M. Maddox and K. E. Gubbins, J. Chem. Phys. **107**, 9659 (1997).

²³H. Kanda, M. Miyahara, and K. Higashitani, Langmuir **16**, 8529 (2000).

²⁴M. Sliwinski-Bartkowiak, G. Dudziak, R. Sikorski, R. Gras, R. Radhakrishnan, and K. E. Gubbins, J. Chem. Phys. **114**, 950 (2001).

²⁵J. Hoffmann and P. Nielaba, Phys. Rev. E **67**, 036115 (2003).

²⁶F. R. Hung, G. Dudziak, M. Sliwinski-Bartkowiak, and K. E. Gubbins, Mol. Phys. **102**, 223 (2004).

²⁷M. Sliwinski-Bartkowiak, F. R. Hung, E. E. Santiso, B. Coasne, G. Dudziak, F. R. Siperstein, and K. E. Gubbins, Adsorption **11**, 391 (2005).

²⁸A preliminary report of these results was presented in Ref. 27.

²⁹B. K. Peterson, J. P. R. B. Walton, and K. E. Gubbins, J. Chem. Soc., Faraday Trans. 2 **82**, 1789 (1986).

³⁰W. A. Steele, Surf. Sci. **36**, 317 (1973).

³¹W. A. Steele, *The Interaction of Gases with Solid Surfaces* (Pergamon, Oxford, 1974).

³²D. A. Kofke, J. Chem. Phys. **98**, 4149 (1993); R. Agrawal and D. A. Kofke, Mol. Phys. **85**, 43 (1995).

³³Q. Yan and J. J. de Pablo, J. Chem. Phys. **111**, 9509 (1999).

³⁴D. Frenkel and B. Smit, *Understanding Molecular Simulation: From Algorithms to Applications*, 2nd ed. (Academic, London, 2002).

³⁵D. A. Kofke, J. Chem. Phys. **117**, 6911 (2002).

³⁶Y. Sugita, A. Kitao, and Y. Okamoto, J. Chem. Phys. **113**, 6042 (2000).

³⁷R. Faller, Q. Yan, and J. J. de Pablo, J. Chem. Phys. **116**, 5419 (2002).

³⁸P. R. ten Wolde, M. J. Ruiz-Montero, and D. Frenkel, J. Chem. Phys. **104**, 9932 (1996); R. M. Lynden-Bell, J. S. van Duijneveldt, and D. Frenkel, Mol. Phys. **80**, 801 (1993); J. S. van Duijneveldt and D. Frenkel, J. Chem. Phys. **96**, 4655 (1992).

³⁹P. J. Steinhardt, D. R. Nelson, and M. Ronchetti, Phys. Rev. B **28**, 784 (1983).

⁴⁰C. G. Gray and K. E. Gubbins, *Theory of Molecular Liquids* (Clarendon, Oxford, 1984).

⁴¹L. D. Landau and E. M. Lifshitz, *Quantum Mechanics* (Pergamon, New York, 1965).

⁴²A. K. Soper, F. Bruni, and M. A. Ricci, J. Chem. Phys. **109**, 1486 (1998); A. K. Soper, J. Phys.: Condens. Matter **9**, 2399 (1997).

⁴³D. Morineau and C. Alba-Simionesco, J. Chem. Phys. **118**, 9389 (2003).

⁴⁴P. Gallo, M. A. Ricci, and M. Rovere, J. Chem. Phys. **116**, 342 (2002).

⁴⁵L. D. Landau and E. M. Lifshitz, *Statistical Physics*, 3rd ed. (Pergamon, London, 1980).

⁴⁶R. Radhakrishnan and B. L. Trout, J. Chem. Phys. **117**, 1786 (2002).

⁴⁷M. Ferrenberg and R. H. Swendsen, Phys. Rev. Lett. **61**, 2635 (1988); **63**, 1195 (1989).

⁴⁸W. H. Press, W. T. Vetterlin, S. A. Teukolsky, B. P. Flannery, *Numerical Recipes in Fortran 77*, 2nd ed. (Cambridge, New York, 2001).

⁴⁹B. K. Peterson and K. E. Gubbins, Mol. Phys. **62**, 215 (1987).

⁵⁰R. Radhakrishnan and K. E. Gubbins, Phys. Rev. Lett. **79**, 2847 (1997).

⁵¹F. R. Hung, B. Coasne, K. E. Gubbins, F. R. Siperstein, and M. Sliwinski-Bartkowiak (unpublished).

- ⁵²M. Miyahara, H. Kanda, M. Shibao, and K. Higashitani, *J. Chem. Phys.* **112**, 9909 (2000); H. Kanda, M. Miyahara, and K. Higashitani, *J. Chem. Phys.* **120**, 6173 (2004).
- ⁵³C. Ghatak and K. G. Ayappa, *Phys. Rev. E* **64**, 051507 (2001); K. G. Ayappa and C. Ghatak, *J. Chem. Phys.* **117**, 5373 (2002).

- ⁵⁴A. Vishnyakov and A. V. Neimark, *J. Chem. Phys.* **118**, 7585 (2003).
- ⁵⁵A. Patrykiewicz, L. Sałamacha, and S. Sokołowski, *J. Chem. Phys.* **118**, 1891 (2003).
- ⁵⁶H. Bock, K. E. Gubbins, and K. G. Ayappa, *J. Chem. Phys.* **122**, 094709 (2005).